

Meandering flows and dynamical vortex glasses in disordered polar active matter

Amélie Chardac,¹ Suraj Shankar,² M. Cristina Marchetti,³ and Denis Bartolo¹

¹*Univ. Lyon, ENS de Lyon, Univ. Claude Bernard,
CNRS, Laboratoire de Physique, F-69342, Lyon, France*

²*Department of Physics, Harvard University, Cambridge, MA 02138, USA*

³*Department of Physics, University of California Santa Barbara, Santa Barbara, CA 93106, USA*

(Dated: November 25, 2021)

Over the past ten years, we have learned how to drive fluids from within by assembling soft matter from motile units [1–8]. We now have a clear understanding of the mesmerizing flows observed in homogeneous active fluids as diverse as bacteria suspensions, microtubule nematics, and colloidal flocks [9–11]. By contrast, our fundamental knowledge of active matter in challenging environments, although crucial to any practical applications, remains virtually uncharted [12–18]. Here, combining active-colloid experiments and theory, we demonstrate and elucidate the amorphous meandering flows of polar liquids frustrated by disorder. Increasing disorder, quenched topological defects proliferate, bend the polar flows, and realize a dynamical vortex glass where flocking motion is only locally preserved. Beyond the specifics of polar liquids, we expect this generic mechanism to shape the random flows of a broad class of active matter ranging from synthetic active nematics to collection of living cells exploring heterogeneous media.

In our experiments we challenge the flows of a prototypical colloidal active fluid with random lattices of micro-fabricated obstacles, and demonstrate an unanticipated phase of active matter. Following [4, 14], we take advantage of the Quincke mechanism to turn inanimate polystyrene beads of radius $a = 2.4 \mu\text{m}$ into colloidal rollers self-propelling at $\sim 1 \text{ mm/s}$ in circular microfluidic chambers of radius $R = 1.5 \text{ mm}$. Before addressing the impact of disorder, it is worth recalling the phenomenology of the pure system. Working with an area fraction of $\rho = 7 \times 10^{-2}$, as the rollers are set in motion, they interact and self-assemble into a spontaneously flowing liquid commonly referred to as a Toner–Tu fluid or a polar liquid [4, 9, 19], see Supplementary Video 1. The resulting flow patterns are initially isotropic and marred by a number of topological defects clearly visible in the Schlieren patterns of Fig. 1a and Supplementary Video 2. However, the velocity-alignment interactions responsible for flocking motion penalize flow distortions thereby causing the attraction and annihilation of topological defects of opposite charges. The resulting lively coarsening dynamics lasts few tens of seconds and ultimately yields pristine azimuthal flows.

Disorder is implemented by random lattices of isotropic obstacles of diameter $10 \mu\text{m}$ that repel the rollers at a distance, while leaving their speed unaltered, see Fig. 1b

and Supplementary Video 3. Starting with a pure system deep in the ordered phase, we repeat the experiments increasing the obstacle fraction Φ_o from 1% to 38% keeping the system below the Lorentz localization transition of individual rollers [20]. For small disorder ($\Phi_o < 9\%$), the obstacles hardly alter the coarsening dynamics and merely cause smooth distortions of the flow field centered around a single $+1$ defect, see Fig. 1 and Supplementary Video 4. In stark contrast, increasing Φ_o above 9%, a very distinct class of static patterns emerges. Even though orientational order locally subsists, disorder prevents polar interactions from annihilating the ± 1 defects formed at the onset of collective motion, Fig. 1d. As exemplified in Fig. 1c and Supplementary Video 5, the streamlines then form static meandering patterns bent by a finite density of pinned topological defects. Further increasing the obstacle fraction (above 26%), we recover the phenomenology reported in [14]. Disorder suppresses the flocking transition and the interacting rollers form an active isotropic gas. The associated flows are highly dynamical as a host of defect pairs continuously unbind and annihilate, see Figs. 1c, 1d and Supplementary Video 6. The two transitions between the three dynamical states are unambiguously determined by the variations of the mean number of topological defects of the velocity field $\mathcal{N}(\Phi_o)$ plotted in Fig. 1e (the detection of the topological defects is detailed in Supplementary Note II). The emergence of meandering flows is signalled by the linear increase of \mathcal{N} as Φ_o exceeds the critical value $\Phi_c = 9\%$, whereas the loss of local orientational order saturates $\mathcal{N}(\Phi_o)$ above $\Phi_o = 26\%$. In order to quantitatively distinguish the three regimes, we inspect the statistics of the time-averaged polarization defined as $\mathbf{p}(\mathbf{r}) = \langle \hat{\mathbf{v}}(\mathbf{r}, t) \rangle_t$, where the unit vector $\hat{\mathbf{v}}(\mathbf{r}, t)$ is the instantaneous orientation of the velocity, see Methods. The distributions of $\mathbf{p}(\mathbf{r})$ in Fig. 2a show that, for small disorder, the flow is uniformly and maximally polarized along the azimuthal direction thereby reflecting nearly perfect polar order over system-spanning scales. Conversely, above Φ_c macroscopic polar order is suppressed, and the polarization is isotropically distributed. The strong localization of the distribution on the unit circle demonstrates, however, that meanders persistently distort the streamlines *without* arresting the local flows. Above $\Phi_o = 26\%$, in the active-gas phase, the typical polarization vanishes as flows are suppressed at all scales. We now demonstrate that the two flowing patterns correspond to two distinct phases of active matter. We first

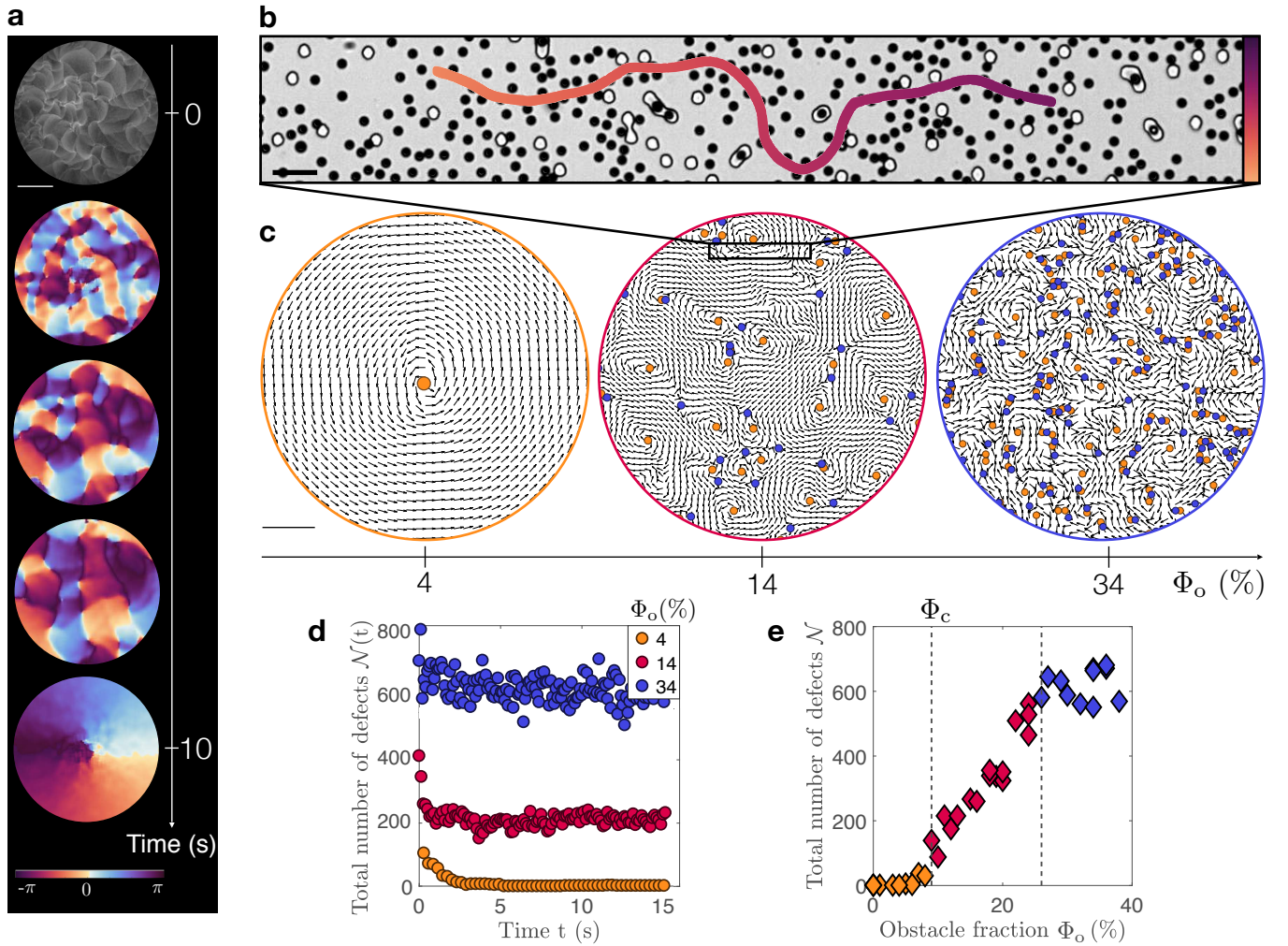


FIG. 1. **Emergence and destruction of polar flows.** **a**, Experimental picture of a Quincke-roller fluid at the onset of self-propulsion and subsequent Schlieren patterns of the flow field. The colormap indicates the angle made by the local velocity field with the x -axis. The many topological defects formed at the onset of collective motion coarsen yielding a pristine azimuthal flow. Scale bar: 1 mm. **b**, Closeup picture showing Quincke rollers collectively moving through a disordered lattice of micro-fabricated obstacles. The roller trajectories show that the obstacles repel the rollers at a finite distance. Scale bar: $50\ \mu\text{m}$. Color bar: time, from the oldest positions (bright colors) to the latest positions (dark colors). **c**, Polarization fields in the vortex, meander and gas states. The dots indicate the location of the topological defects (Orange: $+1$, Blue: -1). Scale bar: $0.5\ \text{mm}$. **d**, Evolution of the number of topological defects $\mathcal{N}(t)$ during the coarsening process for $\Phi_o = 4\%$ (Polar liquid), $\Phi_o = 14\%$ (Meander), $\Phi_o = 34\%$ (Gas). **e**, Variations of the average number of topological defects in the steady state with the obstacle fraction. The meander phase emerges at $\Phi_c = 9 \pm 1\%$.

stress that polar liquids with genuine long range orientational order survive at finite disorder (see also Supplementary Note VB). Unlike active nematics, deconfining the system does not suppress the stationary vortex patterns shown in Fig. 1c [21–23]. This crucial result follows from the finite-size analysis of the polarization order parameter $\mathcal{P}(\ell) = \sqrt{\langle p_r(\mathbf{r}) \rangle_{\mathbf{r}}^2 + \langle p_\theta(\mathbf{r}) \rangle_{\mathbf{r}}^2}$, where ℓ is the size of the region where spatial averaging is performed. This definition of \mathcal{P} is natural in a circular geometry where the spatial average of \mathbf{p} vanishes, even in pure systems. Below Φ_c , Fig. 2b clearly indicates that $\mathcal{P}(\ell)$ converges to a finite value over a finite length scale $\xi_{\mathcal{P}}$, signalling

long range polar order. Conversely, deep in the meandering regime $\mathcal{P}(\ell)$ vanishes over a finite scale. Polar liquids and meanders are therefore two genuinely distinct phases of active matter.

The transition between these two dynamical phases is captured by $\mathcal{P} \equiv \mathcal{P}(\ell = 2R)$, where R is the chamber radius. We show in Fig. 2c that \mathcal{P} decays weakly and linearly with Φ_o for small disorder, but drops sharply to 0 at the critical value Φ_c defined from the proliferation of quenched topological defects in Fig 1e. The bifurcation of \mathcal{P} in Fig. 2c suggests a critical scenario. This hypothesis is further supported by Fig. 2d which

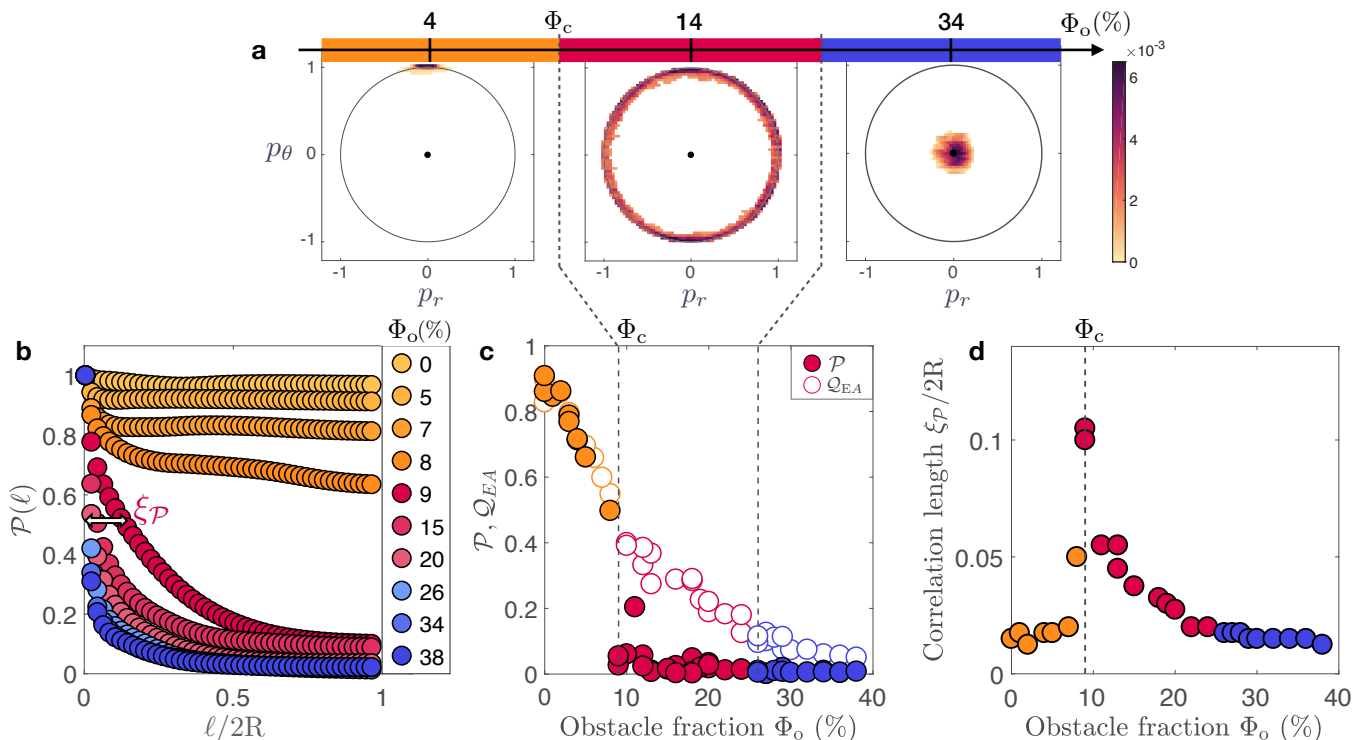


FIG. 2. **Suppression of long-range orientational order.** **a**, PDF of the polarization fields $P(p_r, p_\theta)$ in the three dynamical phases state. Note that the distribution is isotropic but peaked along the unit circle in the meander phase: spontaneous flows are locally preserved but global polar order is suppressed by disorder. **b**, Finite-size analysis of the polarization order parameter $\mathcal{P}(\ell)$ measured in square boxes of width ℓ . The polarization decays exponentially towards a finite value in the polar-liquid phase ($\Phi_o < \Phi_c$) demonstrating the existence of genuine long-range orientational order. No polar order is observed above Φ_c . The chamber diameter $2R$ is 3 mm. **c**, Variation of the global polarization \mathcal{P} and Edwards–Anderson \mathcal{Q}_{EA} order parameters. The polar liquid phase is defined by $\mathcal{P} > 0$, the meander phase by $\mathcal{P} = 0$, $\mathcal{Q}_{EA} > 0$ and the gas phase by $\mathcal{Q}_{EA} = 0$. **d**, Correlation length of the polarization field defined from the exponential decay of $\mathcal{P}(\ell)$ as sketched in (b). The cusp of the $\xi_P(\Phi_o)$ curve at Φ_c hints towards a critical dynamical transition.

reveals a divergence, or at the very least a drastic increase of the correlation length ξ_P at the onset of meandering motion. The polarization \mathcal{P} alone, however, does not distinguish the meander from the gas phase. We thus introduce the Edwards–Anderson parameter $\mathcal{Q}_{EA} = \langle \hat{\mathbf{v}}(\mathbf{r}, t) \cdot \hat{\mathbf{v}}(\mathbf{r}, t + T) \rangle_{\mathbf{r}, t, T \rightarrow \infty}$ that quantifies the temporal persistence of the emergent flows [24]. The finite non-zero value of \mathcal{Q}_{EA} for $\Phi_c < \Phi_o < 26\%$ (Fig. 2c) confirms the persistence of polar order along the meanders. We also find that the continuous transition between the meander and the gas phase, where $\mathcal{Q}_{EA} \sim 0$, coincides with that identified from the topological defect statistics in Fig. 1e.

In order to elucidate how disorder and topological defects conspire to shape the meandering flows, we compare the patterns of fifty replicas of the very same experiment ($\Phi_o = 15\%$). We solely vary the initial conditions, keeping the colloid fraction and disorder realization identical. The resemblance between the flow patterns is quantified by introducing the local overlap $q_{\alpha\beta}(\mathbf{r}) = \mathbf{p}_\alpha(\mathbf{r}) \cdot \mathbf{p}_\beta(\mathbf{r})$ between the replicas α and β . Examples of overlap maps are shown in Fig. 3a for four different pairs of experi-

ments, see also Supplementary Fig. S5. The replicated flows are identical when $q_{\alpha\beta}(\mathbf{r}) = +1$, opposite when $q_{\alpha\beta}(\mathbf{r}) = -1$ and orthogonal when $q_{\alpha\beta}(\mathbf{r}) = 0$. A simple inspection of the maps readily indicates that all experiments correspond to a different pattern, yet few macroscopic regions are virtually identical from one replica to another. More quantitatively, we plot in Fig. 3c the distribution of the global overlap $\mathcal{Q}_{\alpha\beta} = \langle q_{\alpha\beta}(\mathbf{r}) \rangle_{\mathbf{r}}$, and compare it to that of a pure vortex. The two distributions are markedly different. In the pure case, $P(\mathcal{Q}_{\alpha\beta})$ is composed of two identical peaks at $\mathcal{Q}_{\alpha\beta} = \pm 1$, as vortices of opposite handedness are equally probable. In the meander phase, however, $P(\mathcal{Q}_{\alpha\beta})$ is not symmetric. It is a broad Gaussian distribution centered around a positive mean value. In other words, even though disorder is isotropic and homogeneous, the obstacles determine the orientation of the flow field over macroscopic regions of space as illustrated by the replica-averaged velocity field shown in Fig 3b. The large width of the overlap distribution demonstrates a broad class of meandering patterns that do not merely differ from each others by continuous distortions. The replicas are topologically nonequivalent,

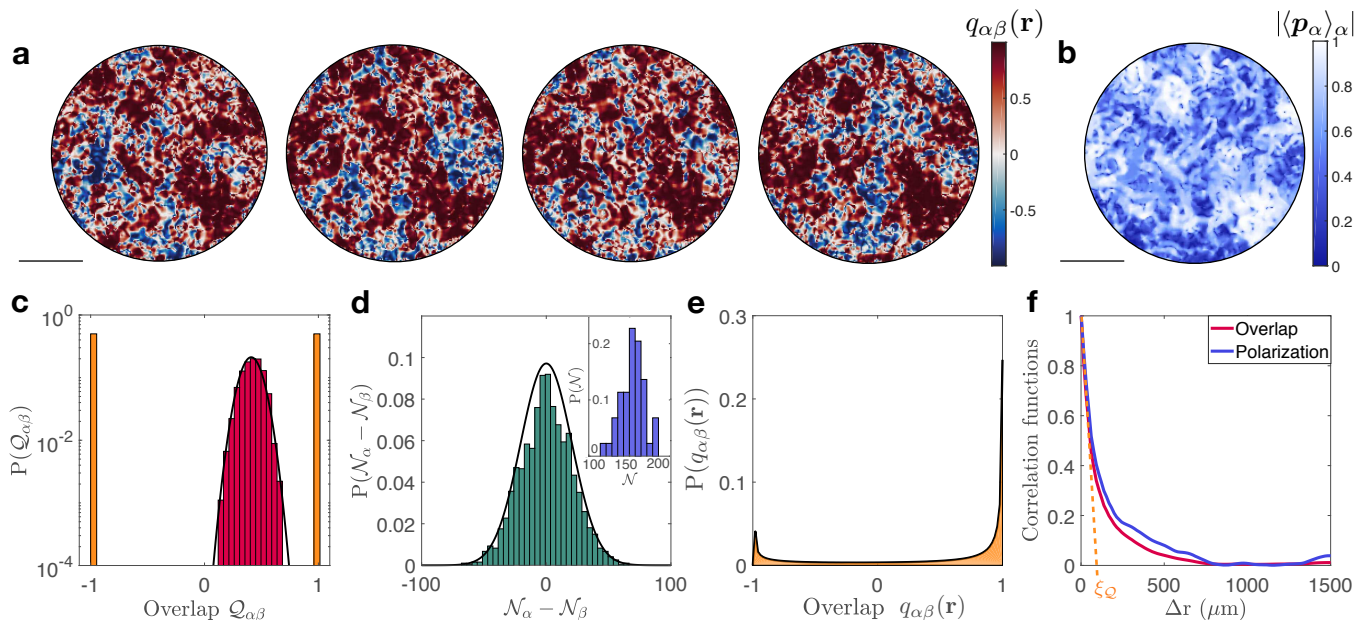


FIG. 3. **Meanders as dynamical vortex glasses.** **a**, Maps of the overlap field $q_{\alpha\beta}(\mathbf{r})$ for 4 out of 1225 different pairs of replicas (α, β). Scalebar: 1 mm. **b**, Magnitude of the replica-averaged polarization field. Disorder robustly sets the flow orientation in macroscopic regions (light colors). Scalebar: 1 mm. **c**, Overlap distributions in the polar liquid and meander phases. In the polar liquid phase (light orange) the distribution is symmetric and bimodal. Clockwise and counterclockwise vortices are equiprobable. In the meander phase, the distribution is a wide Gaussian centered on 0.46. **d**, Distribution of the difference between the number of topological defects in each pair of replicas. The distribution is a Gaussian with a standard deviation $\sigma = 18 \pm 3$ much larger than the uncertainty defined by the standard deviation of the topological charge (which should be constrained to equal 1 in a circular geometry). Inset: distribution of the number of defects in each replica. The replicated flows are topologically distinct. **e**, Probability density of the local overlap $q_{\alpha\beta}(\mathbf{r})$. The distribution is asymmetric but sharply peaked at ± 1 . Locally the active fluid either flows along identical or opposite directions in each replica of the same experiment. **f**, Decay of the spatial correlation of $q_{\alpha\beta}(\mathbf{r})$ averaged over all replicas and of the replica-averaged polarization field plotted in (b). Both decorrelations occur over the same finite distance $\xi_Q = 100 \pm 10 \mu\text{m}$. All panels correspond to experiments performed deep in the meander phase $\Phi_o = 15\%$.

as demonstrated in Fig. 3d showing the distribution of the difference $N_\alpha - N_\beta$ in the number of topological-defect between each pair of replicas. The regions of the flow patterns that are robust to variations in the initial conditions are therefore shaped by pinned defects of identical charge and orientation that persist in all replicas. In other words defects are strongly correlated not only in their spatial location, but also in their flow direction. This becomes evident upon inspecting the local overlap statistics. Unlike the global overlap distribution, $P(q_{\alpha\beta}(\mathbf{r}))$ is bimodal and sharply peaks at $q_{\alpha\beta}(\mathbf{r}) = \pm 1$, see Fig. 3e. Simply put, the meanders in each pair of replicas differ by the reversal of the flow orientation over a finite fraction of space. This area fraction is given by $1 - [P(q_{\alpha\beta} = +1) - P(q_{\alpha\beta} = -1)] \sim 0.5$, see also Supplementary Note III. We can now estimate the typical extent of the compact regions where the flow can flip sign from one replica to another by measuring the correlation length of the local overlap, or of the replica-averaged flow, see Fig. 3f. We find that the overlap decorrelates exponentially over a finite distance $\xi_Q = 100 \pm 10 \mu\text{m}$. This finite correlation length implies that the meanders

explore a conformational landscape including a number of steady states that scales as $\sim 2^{(R/\xi_Q)^2}$. The meander phase is the dynamical analogue of a topological defect glass. It is strongly reminiscent of the vortex glass phases found in disordered flux lines in superconductors and in random-gauge Heisenberg magnets [25–27].

To elucidate the emergence of the meandering patterns we construct a hydrodynamic theory of disordered polar flows. To do so, we build on a final observation: no meander phase emerges in periodic lattices of obstacles, see Supplementary Note IV. The spatial heterogeneities in the local obstacle fraction $\phi_o(\mathbf{r})$ are essential to the bending of the flow patterns. At lowest order in gradients, disorder thus alters Toner–Tu hydrodynamics as:

$$\partial_t \mathbf{v} + \lambda \mathbf{v} \cdot \nabla \mathbf{v} = (a_2 - a_4 v^2) \mathbf{v} + K \Delta \mathbf{v} - \beta \nabla \rho - \beta_o \nabla \phi_o(\mathbf{r}), \quad (1)$$

where all coefficients are positive hydrodynamic constants. When $\nabla \phi_o = \mathbf{0}$, Eq. 1 reduces to the standard Toner–Tu equation which quantitatively predicts the vortical flows of Fig. 1a [28]. The β_o term reflects the coupling to disorder and provides a direct qualita-

tive explanation for the bias of the overlap distribution in Fig. 3c. Although the obstacles are isotropic and, on average, homogeneously distributed, $\phi_o(\mathbf{r})$ acts as a random pressure field that locally drives the flows along the same obstacle-depleted regions in all replicas. However, disorder has a finite magnitude and competes with both the convective (λ) and elastic (K) terms in Eq. 1. Within a linear-response approximation, this competition results in a linear decrease of the polarization in agreement with our experimental measurements in the small disorder limit ($\Phi_o < \Phi_c$), see Fig. 2c and Supplementary Note V. Going beyond the spin-wave approximation, we now introduce an effective-energy picture that rationalizes the existence of the meander phase as a vortex glass. At long wavelengths, the convective nonlinearities solely compete with the random pressure term in Eq. 1. To gain some insight on this competition, let us first consider a local minimum of $\phi_o(\mathbf{r})$ at the origin, the inward disorder pressure must be balanced by a centrifugal kinematic pressure $\sim \lambda v^2/r$ associated with an azimuthal flow. In the limit of a maximally polarized fluid where $\mathbf{v} = v_0(\cos\theta, \sin\theta)$, this competition constrains the angular fluctuations to obey $\nabla\theta = -(\beta_o/\lambda v_0^2)\hat{\mathbf{z}} \times \mathbb{P} \cdot \nabla\phi_o \equiv \mathcal{A}(\mathbf{r})$, where $\mathbb{P} = \mathbf{1} - \hat{\mathbf{v}}\hat{\mathbf{v}}$. Remarkably, this quenched distribution of phase distortions is reminiscent to random-gauge XY models, and flux-line glasses in type II superconductors, see e.g. [26, 27, 29]. \mathcal{A} acts as a random $U(1)$ gauge field, and its local circula-

tion $Q(\mathbf{r}) = \hat{\mathbf{z}} \cdot \nabla \times \mathcal{A}(\mathbf{r})$ defines the quenched topological charge in the background. The polar fluid hence navigates the obstacles, generating meanders dictated by \mathcal{A} , while elasticity penalizes these distortions. The resulting competition allows a Kosterlitz-Thouless style argument for proliferating free vortices, through a mapping to the random XY model ground state (Supplementary Notes VI and VII). The elastic penalty of an isolated defect $\sim K \ln(R/a)$ (a is a core size) can be offset by the energy gain $\sim K\Phi_o(\beta_o/\lambda v_0^2) \ln(R/a)$ from optimally screening out the background charge. Their balance hence predicts a critical threshold $\Phi_c \propto \lambda v_0^2/\beta_o$ beyond which pinned vortices proliferate, in agreement with our experimental findings.

We emphasize the generality of our predictions. Although established for a polar liquid, we expect the distortion of uniaxial flows into a vortex glass phase to be a generic feature of active fluids challenged by isotropic disorder. Both the topological-defect stabilisation scenario and the extensive complexity of the flow patterns solely rely on stable uniaxial order in a fluid assembled from motile units. We therefore expect dynamical vortex glasses to emerge in a host of active materials ranging from confined microtubule nematics [11], to concentrated bacteria suspensions [21], and cell tissues [30] cruising through disorder. Establishing a quantitative theory of their meandering patterns, however, remains a formidable challenge.

-
- [1] Christopher Dombrowski, Luis Cisneros, Sunita Chatkaew, Raymond E. Goldstein, and John O. Kessler, “Self-concentration and large-scale coherence in bacterial dynamics,” *Phys. Rev. Lett.* **93**, 098103 (2004).
- [2] Volker Schaller, Christoph Weber, Christine Semmrich, Erwin Frey, and Andreas R. Bausch, “Polar patterns of driven filaments,” *Nature* **467**, 73 (2010).
- [3] Tim Sanchez, Daniel T. N. Chen, Stephen J. DeCamp, Michael Heymann, and Zvonimir Dogic, “Spontaneous motion in hierarchically assembled active matter,” *Nature* **491**, 431–434 (2012).
- [4] Antoine Bricard, Jean-Baptiste Caussin, Nicolas Desreumaux, Olivier Dauchot, and Denis Bartolo, “Emergence of macroscopic directed motion in populations of motile colloids,” *Nature* **503** (2013).
- [5] Jing Yan, Ming Han, Jie Zhang, Cong Xu, Erik Luijten, and Steve Granick, “Reconfiguring active particles by electrostatic imbalance,” *Nature materials* **15**, 1095 (2016).
- [6] Oleg D. Lavrentovich, “Active colloids in liquid crystals,” *Current Opinion in Colloid & Interface Science* **21** (2016).
- [7] Daiki Nishiguchi and Masaki Sano, “Mesoscopic turbulence and local order in janus particles self-propelling under an ac electric field,” *Phys. Rev. E* **92**, 052309 (2015).
- [8] Chong Chen, Song Liu, Xia-qing Shi, Hugues Chaté, and Yilin Wu, “Weak synchronization and large-scale collective oscillation in dense bacterial suspensions,” *Nature* **542**, 210 (2017).
- [9] M. C. Marchetti, J. F. Joanny, S. Ramaswamy, T. B. Liverpool, J. Prost, Madan Rao, and R. Aditi Simha, “Hydrodynamics of soft active matter,” *Rev. Mod. Phys.* **85**, 1143–1189 (2013).
- [10] John Toner, Yuhai Tu, and Sriram Ramaswamy, “Hydrodynamics and phases of flocks,” *Annals of Physics* **318**, 170 – 244 (2005), special Issue.
- [11] Amin Doostmohammadi, Jordi Ignés-Mullol, Julia M Yeomans, and Francesc Sagués, “Active nematics,” *Nature communications* **9**, 1–13 (2018).
- [12] Oleksandr Chepizhko, Eduardo G. Altmann, and Fernando Peruani, “Optimal noise maximizes collective motion in heterogeneous media,” *Phys. Rev. Lett.* **110**, 238101 (2013).
- [13] David A Quint and Ajay Gopinathan, “Topologically induced swarming phase transition on a 2d percolated lattice,” *Physical biology* **12**, 046008 (2015).
- [14] Alexandre Morin, Nicolas Desreumaux, Jean-Baptiste Caussin, and Denis Bartolo, “Distortion and destruction of colloidal flocks in disordered environments,” *Nature Physics* **13**, 63 (2017).
- [15] Rakesh Das, Manoranjan Kumar, and Shradha Mishra, “Polar flock in the presence of random quenched rotators,” *Phys. Rev. E* **98**, 060602 (2018).
- [16] CJ Olson Reichhardt and Charles Reichhardt, “Avalanche dynamics for active matter in heterogeneous media,” *New Journal of Physics* **20**, 025002 (2018).

- [17] John Toner, Nicholas Guttenberg, and Yuhai Tu, “Swarming in the dirt: Ordered flocks with quenched disorder,” *Phys. Rev. Lett.* **121**, 248002 (2018).
- [18] John Toner, Nicholas Guttenberg, and Yuhai Tu, “Hydrodynamic theory of flocking in the presence of quenched disorder,” *Phys. Rev. E* **98**, 062604 (2018).
- [19] John Toner and Yuhai Tu, “Long-range order in a two-dimensional dynamical XY model: How birds fly together,” *Phys. Rev. Lett.* **75**, 4326–4329 (1995).
- [20] Alexandre Morin, David Lopes Cardozo, Vijayakumar Chikkadi, and Denis Bartolo, “Diffusion, subdiffusion, and localization of active colloids in random post lattices,” *Phys. Rev. E* **96**, 042611 (2017).
- [21] Hugo Wioland, Enkeleida Lushi, and Raymond E Goldstein, “Directed collective motion of bacteria under channel confinement,” *New Journal of Physics* **18**, 075002 (2016).
- [22] Kun-Ta Wu, Jean Bernard Hishamunda, Daniel TN Chen, Stephen J DeCamp, Ya-Wen Chang, Alberto Fernández-Nieves, Seth Fraden, and Zvonimir Dogic, “Transition from turbulent to coherent flows in confined three-dimensional active fluids,” *Science* **355**, eaal1979 (2017).
- [23] Achini Opathalage, Michael M Norton, Michael PN Juniper, Blake Langeslay, S Ali Aghvami, Seth Fraden, and Zvonimir Dogic, “Self-organized dynamics and the transition to turbulence of confined active nematics,” *Proceedings of the National Academy of Sciences* **116**, 4788–4797 (2019).
- [24] Andrea Cavagna, “Supercooled liquids for pedestrians,” *Physics Reports* **476**, 51–124 (2009).
- [25] Matthew P. A. Fisher, “Vortex-glass superconductivity: A possible new phase in bulk high- t_c oxides,” *Phys. Rev. Lett.* **62**, 1415–1418 (1989).
- [26] Thomas Nattermann and Stefan Scheidl, “Vortex-glass phases in type-II superconductors,” *Advances in Physics* **49**, 607–704 (2000).
- [27] David Carpentier and Pierre Le Doussal, “Topological transitions and freezing in xy models and coulomb gases with quenched disorder: renormalization via traveling waves,” *Nuclear Physics B* **588**, 565–629 (2000).
- [28] Antoine Bricard, Jean-Baptiste Caussin, Debasish Das, Charles Savoie, Vijayakumar Chikkadi, Kyohei Shitara, Oleksandr Chepizhko, Fernando Peruani, David Saintillan, and Denis Bartolo, “Emergent vortices in populations of colloidal rollers,” *Nature communications* **6**, 7470 (2015).
- [29] Michael Rubinstein, Boris Shraiman, and David R Nelson, “Two-dimensional xy magnets with random dzyaloshinskii-moriya interactions,” *Physical Review B* **27**, 1800 (1983).
- [30] G Duclos, C Blanch-Mercader, V Yashunsky, G Salbreux, J-F Joanny, J Prost, and Pascal Silberzan, “Spontaneous shear flow in confined cellular nematics,” *Nature physics* **14**, 728–732 (2018).
- [31] J. R. Melcher and G. I. Taylor, “Electrohydrodynamics: A review of the role of interfacial shear stresses,” *Annual Review of Fluid Mechanics* **1**, 111–146 (1969).
- [32] Peter J Lu, Peter A Sims, Hidekazu Oki, James B Macarthur, and David A Weitz, “Target-locking acquisition with real-time confocal (tarc) microscopy,” *Optics express* **15**, 8702–8712 (2007).
- [33] John C Crocker and David G Grier, “Methods of digital video microscopy for colloidal studies,” *Journal of colloid and interface science* **179**, 298–310 (1996).
- [34] D. Blair and E. Dufresne, “The matlab particle tracking code repository” .

METHODS

A. Quincke rollers experiments

The experimental setup is similar to that described in [14]. We disperse polystyrene colloids of radius $a = 2.4\ \mu\text{m}$ (Thermo Scientific G0500) in a solution of hexadecane including 5.5×10^{-2} wt% of dioctyl sulfosuccinate sodium salt (AOT). We then inject the solution in microfluidic chambers made of two electrodes spaced by a $25\ \mu\text{m}$ -thick scotch tape. The electrodes are glass slides, coated with indium tin oxide (Solems, ITOSOL30, thickness: 80 nm). We let the colloids sediment on the bottom electrode and apply a DC voltage of 120 V. The resulting electric field triggers the so-called Quincke electro-rotation and causes the colloids to roll at a constant speed $v_0 = 0.8\ \text{mm/s}$ [4, 31]. We confine the colloidal rollers inside circular chambers of radius $R = 1.5\ \text{mm}$ including random lattices of circular posts of radius $10\ \mu\text{m}$. Both the obstacles and the confining disks are made of a $2\ \mu\text{m}$ -thick layer of insulating photoresist resin (Microposit S1818) patterned by means of conventional UV-Lithography as explained in [14]. The patterns are lithographed on the bottom electrode. Note that the distribution of the obstacle centers corresponds to a planar Poisson process, the circular posts can therefore overlap as see in Fig. 1b and Supplementary Video 3.

The experiments reported in the main text correspond to thirty different microfluidic chambers including obstacle fractions ranging from 0% to 38%. If not specified otherwise, the stationary flows are measured in the first chamber 120 s after the application of the DC field. This waiting time is more than one order of magnitude larger than the flows’ relaxation time, see Supplementary Note I. For the replica experiments we proceed as follows: the chambers are filled with the colloids at the desired area fraction. We motorize the colloids, wait for 120 s and film their motion for 5 s. We then switch the voltage off, and switch it on again repeating the same procedure fifty times in a row.

B. From Lagrangian trajectories to Eulerian flow fields

In order to track of the trajectories of the rollers, we image them with a Nikon AZ100 microscope with a 4.8X magnification and record videos with a CMOS camera (Basler Ace) at 190 fps. All measurements are systematically repeated three times for different initial conditions and same disorder configuration. If not specified otherwise, we measure all quantities reported in the main text after the ensemble of rollers has reached

its stationary state.

1. Lagrangian trajectories

We detect the position of all the rollers with a sub-pixel accuracy using the algorithm introduced by Lu et al in [32]. We then reconstruct their trajectories over the whole 3 mm wide circular chambers using the Crocker and Grier algorithm [33] with the MATLAB routine available at [34]. We define the individual roller velocities from their displacements over two subsequent frames (time interval: $\delta t = 5.3$ ms): $\mathbf{v}_i(t) = \mathbf{r}_i(t + \delta t) - \mathbf{r}_i(t)$, where $\mathbf{r}_i(t)$ and $\mathbf{v}_i(t)$ are respectively the position and velocity of particle i at time t . The accuracy of the position measurements is of the order of $0.1 \mu\text{m}$, inducing an accuracy of the order of $40 \mu\text{m/s}$ for individual speed measurements. When powered with an electric field \mathbf{E} of magnitude 120 V, all colloids roll at a constant speed:

$$v_0 = 0.80 \pm 0.04 \text{ mm/s.} \quad (2)$$

In addition, when isolated, their direction of motion freely diffuses on the unit circle with a rotational diffusivity D_R defined as the exponential decorrelation rate of the velocity orientation in an isotropic phase:

$$D_R = 2.2 \pm 0.1 \text{ s}^{-1}. \quad (3)$$

2. Eulerian fields

Building on these Lagrangian measurements, we reconstruct the instantaneous Eulerian velocity fields $\mathbf{v}(\mathbf{r}, t)$ as follows. We average the instantaneous roller velocities in $76.4 \mu\text{m} \times 76.4 \mu\text{m}$ binning windows arranged on a square lattice with a lattice spacing of $15.3 \mu\text{m}$. Given the roller

density, each PIV window typically averages the velocity of 25 rollers. We systematically checked that none of our results crucially depends on the specific choice of the size of the binning windows. The polarization and overlap fields are computed with the same spatial resolution from $\mathbf{v}(\mathbf{r}, t)$.

To compute the polarization order parameter from the instantaneous velocity field, we first average the radial and azimuthal components of the polarization field $\mathbf{p}(\mathbf{r}) \equiv \langle \hat{\mathbf{v}}(\mathbf{r}, t) \rangle_t$ over square boxes of size ℓ . We then compute the spatial average: $\mathbf{p}_B \equiv (\langle p_r(\mathbf{r}) \rangle_{\mathbf{r}}, \langle p_\theta(\mathbf{r}) \rangle_{\mathbf{r}})$, in each box B . Finally, $\mathcal{P}(\ell)$ corresponds to the norm of \mathbf{p}_B averaged over all boxes B .

Acknowledgements. We acknowledge support from ANR program WTF and IDEX program ToRe. M. C. M. was supported by the US National Science Foundation through award DMR-1609208. S. S. is supported by the Harvard Society of Fellows. We thank D. Carpentier, O. Dauchot and A. Morin for insightful comments and suggestions.

Data availability The data that support the plots within this paper and other findings of this study are available from the corresponding author upon request.

Author Contributions D. B. conceived the project. A. C. and D. B. designed the experiments. A. C. performed the experiments and analyzed data. A. C. and D. B. interpreted and discussed the experiments. M. C. M. and S. S. performed the theory. All authors discussed the results and wrote the manuscript. A. C. and S. S. contributed equally.

Author Information Correspondence and requests for materials should be addressed to D. B. (email: denis.bartolo@ens-lyon.fr).

Competing interests The authors declare no competing interests.